Fuel 144 (2015) 71–79

Contents lists available at ScienceDirect

Fuel

journal homepage: www.elsevier.com/locate/fuel

The numerical simulation of biofuels spray

Blaž Vajda [a,*], Luka Lešnik [a], Gorazd Bombek [a], Ignacijo Biluš [a], Zoran Žunič [b], Leopold Škerget [a], Marko Hočevar [c], Brane Širok [c], Breda Kegl [a]

[a] University of Maribor, Faculty for Mechanical Engineering, Engine Research Laboratory, Smetanova ulica 17, SI-2000 Maribor, Slovenia
[b] AVL-AST d.o.o., Trg Leona Štuklja 5, SI-2000 Maribor, Slovenia
[c] University of Ljubljana, Faculty for Mechanical Engineering, Laboratory for Hydraulic Machines, Aškerčeva 6, SI-1000 Ljubljana, Slovenia

HIGHLIGHTS

- Numerical analysis of biofuels' influence on injected fuel-spray cone's angle and length is being analyzed.
- Pressurized chamber with nitrogen at 40–60 bar is used for experimental measurements of spray development.
- The fuels are experimentally investigated in order to verify the numerical model.
- Empirical expressions were developed for fuel properties and engine-operating conditions.
- Experimental and numerical results confirmed the usability of the numerical model.

ARTICLE INFO

Article history:
Received 18 March 2014
Received in revised form 24 November 2014
Accepted 26 November 2014
Available online 16 December 2014

Keywords:
Biofuels
Numerical simulation
Spray shape
Pressure chamber

ABSTRACT

In this paper, the possibility of replacing mineral diesel fuels with different biofuels is analyzed. The study focuses on a numerical investigation of biofuels' influence on an injected fuel-spray cone's angle and length, which have further influence on the combustion process and the formation of pollutants in internal combustion engines. The influence of different physical and chemical properties of pure mineral diesel fuel, biodiesel fuel and their blends on spray characteristics was investigated with the AVL FIRE simulation program. Several different empirical model parameters, usually the engine-operating regime and biofuel used, must be defined when using numerical models. In this study, the numerical model implemented in AVL FIRE was modified so that all model parameters were determined regarding biofuel properties and engine-operating conditions. Experimental measurements of spray development in a cylindrical chamber pressurized with nitrogen at 40–60 bar were performed for validation of the modified numerical model. Photos of spray development were taken with a high speed camera simultaneously with pressure and needle-lift signals. The comparison of experimental and numerical results confirmed the usability of the numerical model. Numerical results of spray development for different biofuels under different operating regimes and ambient pressure confirm the possible usage of biofuels as a replacement for mineral diesel fuel in diesel engines with the early generation of fuel injection systems.

1. Introduction

Global atmospheric pollution has become a serious problem. Competitiveness in the engine industry and rising environmental concerns have increased the research of alternative fuels. It has long been known that biofuels can decrease the pollution from the combustion process in internal combustion engines. Biodiesel is the most frequently used biofuel for decreasing pollution in diesel engines [1–5]. It can be produced from several different raw materials, which influence its physical and chemical properties that are important in the compression ignition engine injection and combustion process. The distribution of fuel droplets and their vaporization in a diesel engine combustion chamber are the dominant factors governing the fuel/air mixture formation, combustion process, engine performance and pollutant formation. The process of spray development and the atomization of biofuels seems to be different in comparison to diesel fuel [6–8].

The influence of different fuel (biofuel) properties on spray characteristics could be investigated experimentally or numerically. Experimental measurements of spray characteristics enable us to see the actual spray development. Numerical analysis (CFD) allows us more detailed investigation into the fuel spray development dynamic and the influence of different fuel properties on

* Corresponding author at: Orešje 124, 2250 Ptuj, Slovenia. Tel.: +386 41 522 145.
E-mail address: bvajda@gmail.com (B. Vajda).

http://dx.doi.org/10.1016/j.fuel.2014.11.090
0016-2361/

droplet formation. Numerical simulations are generally faster and less expensive in comparison to experiments.

When numerical simulations are used, fuel injection in internal combustion engines must be considered as a two-phase flow, which could be simulated using the Euler–Euler or Euler–Lagrange approaches. The Euler–Lagrange approach is more suitable for fuel spray simulations because it treats each fuel droplet as an individual particle. In numerical models, several empirical constants are present, regardless of the approach used. These constants need to be defined before the simulation is started. Values of empirical constants depend on injection system characteristics, engine operating regime, and the physical and chemical properties of the fuel used. The determination of constants is based on users' experiences and might be difficult for the cases in which new biofuels are introduced [9–10].

Many studies on spray development have been performed. Agarwal and Chaudhury [11] experimentally investigated the effect of ambient pressure on spray characteristics in a constant volume spray chamber. The fuels used for the research were Karanja KB100 biodiesel produced from feed-stocks such as Jatropha, KB0 diesel fuel, and KB5 and KB20 blends. The results of their investigation showed that spray tip penetration decreases while the cone angle and spray area increase with the increase of ambient pressure. A similar experimental study was also made by Lee et al. in [12]. They investigated the influence of fuel properties on spray tip penetration, mean droplet size, velocity distribution, and injection profiles using a visualization system and a phase Doppler particle analyzer system. The study was made using different mixing ratios of diesel and biodiesel fuel. The results indicate that the mean size of the droplets increases in accordance with the mixing ratio of the biodiesel fuel. The investigation was made using single-cylinder diesel engine with a common-rail injection system. An engine with a common-rail injection system was also used in the study of Grimaldi and Postrioti [13]. They also used conventional mineral diesel fuel, pure bio-derived fuel and blends of them to investigate the influence on spray characteristics, such as penetration length and spray cone angle. The study was made using two different rail pressures, following which spray jets were injected in the chamber with atmospheric pressure. All presented experimental results indicated that the higher viscosity and surface tension of biofuels result in longer spray penetration lengths and narrower spray jets. Higher ambient pressure results in wider spray cone angles and in decreased spray penetration lengths.

Hohman and Renz [14] used an Euler–Lagrange approach for a numerical study of ambient temperature and pressure influence on the vaporization process of unsteady *n*-heptane and binary model D7N3 fuel sprays. They developed an extended droplet vaporization model that accounts for the effects of non-ideal droplet evaporation and gas solubility. The model includes the diffusion of heat and species within fuel droplets. The model has been implemented into the CFD program FLUENT. The results of the numerical simulation were validated using experimental results, which were made in a high-temperature-high-pressure chamber using a phase-Doppler measurement system. The results comparison shows the influence of pressure and temperature on the vaporization rate of fuel droplets.

The effect of the ambient condition on the droplet atomization characteristics of dimethyl ether fuel was studied experimentally and numerically in the work of Suh et al. [15]. They concluded that smaller droplets are distributed at higher ambient pressures. The Sauther mean diameter of fuel droplets increases when the ambient temperature is increased.

Pogorevc et al. [16] numerically investigated the influence of different biofuels properties on spray tip penetration length and spray cone angle at atmospheric pressure. The aim of this study was to numerically analyze the influence of different physical and chemical properties of biofuels on spray characteristics at various engine operating regimes and different pressures. The numerical model based on the Euler–Lagrange approach was modified in order to make it independent of empirical parameters. For verification of a modified numerical model, several measurements of fuel spray development were performed in a specially designed pressure chamber. The focus of the study is on the possibility of replacing the mineral diesel fuels with different biofuels in the tested diesel engine.

This paper discusses the possibility of replacing mineral diesel fuels with different biofuels. The focus of the study is a numerical investigation of an injected fuel-spray cone's angle and length. In addition to injection system measurements, fuel physical properties and injection process characteristics were measured for pure mineral diesel fuel, biodiesel fuel and their blends. The standard numerical model implemented in AVL FIRE was modified in such a way that all model parameters were determined regarding biofuel properties and engine-operating conditions. For validation purposes, the spray was injected into a cylindrical chamber pressurized with nitrogen at 40–60 bar. Spray macro characteristics were taken with a high-speed camera simultaneously with pressure and needle-lift signals. The comparisons of experimental and numerical results were made using AVL FIRE software and confirm the usability of the developed numerical model. The numerical results of spray development for different biofuels under different operating regimes and ambient pressures confirm the possible usage of biofuels as a replacement for mineral diesel fuel in diesel engines with the early generation of fuel injection systems.

2. Tested fuels

D2 mineral diesel fuel that contained no additives and conformed to European standard EN 590 and B100 biodiesel fuel produced from rapeseed oil at Biogoriva, Rače, Slovenia that conformed to European standard EN 14214, and the D50B50 blends (blend of 50% diesel fuel and 50% biodiesel fuel) and D85E15 (blend of 85% diesel fuel and 15% ethanol) were used in this study. It is well-known that fuel properties have a perceptible influence on injection and engine characteristics. For this reason, all the fluid properties used should be used as a starting parameters for numerical simulations. In this study, the following fluids were used (Table 1).

3. Spray simulations

The spray simulations in this study are based on a statistical method referred to as the discrete droplet method. Droplet parcels are introduced in the flow-domain with initial conditions of position, size, velocity, temperature, and the number of particles in the parcel. The droplets are tracked in the Lagrangian manner through the computational grid used for solving the gas-phase partial differential equations. Full two-way interaction between the gas and liquid phases is taken into account. The basic equation for momentum is [17]:

Table 1
Fluid properties.

Fuel	Density (kg/m^3)	Dynamic viscosity at 20 °C (MPa s)	Surface tension at 20 °C (N/mm)
Mineral diesel D2	827	3.2	26.8
Biodiesel B100	875	6.1	28.4
D50B50	825	4.3	27.6
D85E15	822	2.8	25.4

$$M\frac{du_{id}}{dt} = F_{idr} + F_{ig} + F_{ip} + F_{ib} \tag{1}$$

where m is the mass [kg], u_{id} is the particle velocity vector [m/s], F_{idr} is the drag force [N], F_{ig} is a force including the effects of gravity and buoyancy [N], F_{ip} is the pressure force [N] and F_{ib} summarizes other external forces [N]. Drag force is given by:

$$F_{idr} = D_p|u_{rel}| \tag{2}$$

u_{rel} is the relative velocity [m/s], D_p is the drag function, defined as:

$$D_p = \frac{1}{2}\rho_g A_d C_d |u_{rel}| \tag{3}$$

ρ_g is the fluid density [kg/m^3], C_d is the drag coefficient, which generally is a function of the droplet Reynolds number Re_d, and A_d is the cross-sectional area of the particle [mm].

C_d is calculated by formulation from Schiller and Naumann:

$$C_D = \begin{cases} \frac{24}{Re_d}(1 + 0.15Re_d^{0.687}) \leqq Re_d < 10^3 \\ 0.44 \leqq Re_d \geq 10^3 \end{cases} \tag{4}$$

The particle Reynolds number is shown in the following equation

$$Re_d = \frac{\rho_a |u_{rel}| D_d}{\mu_g} \tag{5}$$

where μ_g is the domain fluid viscosity [MPa s] and where D_d represents the particle diameter [mm].

F_{ig} is a force including the effects of gravity and buoyancy

$$F_{ig} = V_p(\rho_a - \rho_g)g_i \tag{6}$$

V_p is the volume [m^3], ρ_a and ρ_g stand for air and fuel density [kg/m^3] and g_i gravitational acceleration [m/s^2].

F_{ip} is the pressure force, given by

$$F_{ip} = V_p \nabla p \tag{7}$$

where p represents the pressure [Pa] and F_{ib} summarizes other external forces [N]. The forces taken into account in this study are the drag force F_{idr} [N] and the gravitational force F_{ig} [N]. Inserting the above forces and relations into Eq. (1) and dividing it by the particle mass m_d [kg], the equation for the particle acceleration is

$$\frac{du_{ip}}{dt} = \frac{3}{4}\frac{\rho_a}{\rho_d}\frac{1}{D_d}|u_{ia} - u_{ip}|(u_{ia} - u_{ip}) + \left(1 - \frac{\rho_a}{\rho_g}\right)g_i \tag{8}$$

In Eq. (8), ρ_a and ρ_g represent air and fuel density [kg/m^3], D_d is the droplet diameter [mm], the $u_{ia} - u_{ip}$ difference is between the particle and surrounding air velocities [m/s], and g_i represents the acceleration of gravity [m/s^2].

The relation above can be integrated to obtain the particle velocity u_{id} [m/s], and from this the instantaneous particle position vector dx_{ip} [mm] can be determined by integrating:

$$\frac{dx_{ip}}{dt} = u_{id} \tag{9}$$

3.1. Primary break-up model

The main problem for modelling fuel spray atomization is the identification and quantification of the mechanisms governing the relevant break-up processes. For the primary break-up, a core injection model was used (Fig. 1). This model considers two independent mechanisms: aerodynamic surface wave growth and internal stresses by turbulence. For establishing the liquid core erosion rate, locally resolved coupling to the nozzle flow, as well as estimated average values of nozzle flow turbulence, can be taken into account. It is assumed in this model that the turbulent

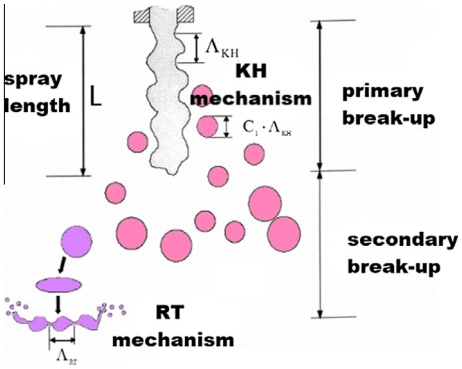

Fig. 1. Definition of primary and secondary (KH and RT mechanism) break-up Regimes [17].

fluctuations in the jet are creating initial perturbations on the jet surface. These grow under the action of aerodynamic pressure forces until they detach as atomized droplets. The coherent liquid core region at the nozzle exit where primary break-up occurs is calculated from a mass balance at the volume elements of the liquid core delivering the core shape [17].

The determination of mass loss from this region is set up using the rate approach

$$\frac{dR}{dt} = \frac{L_A}{\tau_A} \tag{10}$$

where R is the cone radius [mm], τ_A the break time [s], with turbulent length scale L_A calculated from the local values of turbulent kinetic energy and turbulent dissipation

$$L_A = C_2 C_\mu \frac{k^{1.5}}{\varepsilon} \tag{11}$$

in the nozzle exit cross section with constant $C_\mu = 0.09$. The diameter of the product drops resulting from this model is taken as proportional to the turbulent length scale and equal to the atomization length scale.

$$L_A = D_d \tag{12}$$

Thus, droplet size depends on the local values of turbulent kinetic energy and turbulent energy dissipation. The time scale for the break-up is calculated from both mechanisms under consideration, which are the turbulent and aerodynamic break-up, using weighting coefficients C_1 and C_3.

$$\tau_A = C_1\tau_t + C_3\tau_w \tag{13}$$

The turbulent time scale τ_t is calculated from

$$\tau_t = C_\mu \frac{k}{\varepsilon} \tag{14}$$

and the aerodynamic time scale τ_w as characteristic value for the wavelength L_w. This yields

$$\tau_w = L_w\left[\frac{(\rho_a\rho_g u_{rel}^2)}{(\rho_a + \rho_g)} - \frac{\sigma}{(\rho_a + \rho_g)L_w}\right]^{-0.5} \tag{15}$$

where σ defines the surface tension [N/m], ρ_a and ρ_g stand for air and fuel density [kg/m^3], and u_{rel} [m/s] relative velocity.

3.2. Secondary break-up model

In the wave model (Fig. 1), a rate approach for the radius reduction of the parent drops is applied

$$\frac{dr}{dt} = \frac{r_c - r_d}{\tau_{KH}} \tag{16}$$

where r_c is the starting droplet radius [mm], r_d is the stable droplet radius [mm] and τ_{KH} is the break-up time of the model [s], which can be calculated as:

$$\tau_{KH} = \frac{3.726 C_2 r_d}{\Omega_{KH} \Lambda_{KH}} \tag{17}$$

The constant C_2 corrects the characteristic break-up time and varies from one injector to another. r_c is the droplet radius of the product droplet, which is proportional to the wavelength Λ_{KH} of the fastest growing wave on the liquid surface:

$$r_c = C_1 \Lambda_{KH} \tag{18}$$

The wavelength Λ_{RT} and wave growth rate Ω_{RT} depend on the local flow properties.

$$\Lambda_{RT} = \pi \frac{C_4}{K_{RT}} \tag{19}$$

$$\Omega_{RT} = \sqrt{\frac{2}{3\sqrt{3\sigma}} \frac{(-(\vec{g} + \vec{a})(\rho_f - \rho_a))^{1.5}}{\rho_f + \rho_a}} \tag{20}$$

$$K_{RT} = \sqrt{\frac{-(\vec{g} + \vec{a})(\rho_f - \rho_a)}{3\sigma}} \tag{21}$$

The break time and critical radius at RT mechanisms can be defined as

$$\tau_{RT} = \frac{C_5}{\Omega_{RT}} \tag{22}$$

$$r_c = \frac{C_4 \pi}{2 K_{RT}} \tag{23}$$

Break-up length is defined as:

$$L = C_3 \sqrt{\frac{\rho_f}{\rho_a}} d_0 \tag{24}$$

The existing physical–mathematical model for two-phase flows implemented in the commercial CFD code AVL FIRE, and mentioned above, generally yields good results. Several empirical constants of primary and secondary break-up are present in sub-models, and they have significant influence on spray development. They depend on the injection system, fuel properties and the geometry of the injection nozzle. The empirical constants are obtained via experimental–numerical investigation and engineering knowledge. The values of these constants are suitable only for specific injection systems, operating conditions and fuel properties and need to be changed if the fuel type changes. Therefore, finding their right values and achieving accurate spray development can present a problem.

All the above-mentioned deficiencies of the standard physical–mathematical model implemented in the AVL FIRE CFD code led to the improvement of only the primary and secondary break-up model parameters.

4. Primary and secondary break-up model parameters determination

The primary and secondary break-up parameters have a definite and significant impact on the development of spray and its characteristics. They are usually determined based on experiences and simulations made in laboratories. Mainly they depend on the injection system's characteristics, fuel properties, the working regimes and other parameters. Finding their correct values and achieving accurate spray development is a challenge that we tackled using a genetic algorithm.

Table 2
Primary and secondary breakup parameter values.

Fuel	Camshaft rotation speed (rpm)									
	500					1100				
	C_1	C_2	C_3	C_4	C_5	C_1	C_2	C_3	C_4	C_5
D2	14	5	0.2	0.1	0.01	2	2	0.6	0.1	0.01
B100	16	4	0.05	0.1	0.01	3	2	0.14	0.1	0.01

In our case, the parameters C_i (C_1, C_2, C_3, C_4 and C_5) were determined using fuel properties and engine-operating regime information. Their initial values presented in Table 2 were defined using a parametrical study and comparison to experimental spray development.

The break-up model parameters C_i were defined using the following expression depending on fuel properties and engine operating regime:

$$C_i = x_1^{a_1} x_2^{a_2} x_3^{a_3} \ldots \tag{25}$$

where x_i represents fuel properties (density, surface tension, dynamic viscosity, injection pressure), nozzle diameter and working regime. a_i are the appropriate coefficients. The coefficients a_i in Eq. (25) were determined with the usage of Multi-Objective Genetic Algorithm (MOGA) [18].

The algorithm uses a smart multi-search elitism based on Pareto Elitism. This new elitism operator is able to preserve some excellent solutions without causing premature convergence into local optimal fronts. In the case of a single objective, the elitism can be easily defined, identifying it with the operator that preserves and copies the solution with the best fitness to the next generation. The problem of suitably defining the elitism arises in the context of a multi-objective algorithm, where there is more than one objective function and the possibility of more than one elite solution. In the case of multiple objectives, the concept of Pareto optimality should be introduced, as should the correlated idea of dominance; by definition, Pareto solutions are considered optimal because there are no other designs that are superior in all objectives. More formally:

Definition 1 (*Pareto optimal*). Suppose we wish to maximize all f_i a decision vector $x^* \in S$ is Pareto optimal if there is not another decision vector $x \in S$ such that $f_i(x) \geqslant f_i(x^*)$ for all $i = 1, \ldots, k$ and $f_j(x) > f_j(x^*)$ for at least one index j. Mathematically, every Pareto optimal point is an equally acceptable solution for a multi-objective problem.

Definition 2 (*Dominance*). A decision vector x dominates another decision vector y if $f_i(x) \geqslant f_i(y)$ for all i=1,…,k and $f_j(x) \geqslant f_j(y)$ for at least one index j.

Fig. 2 presents a point A in a two-objective (f_1 and f_2) optimization problem. Point A defines two zones: the shaded one (i.e. the left-bottom quadrant) represents the set of the dominated points, while the complementary area (i.e. the whole of the other three quadrants) represents the set of the non-dominated points. If A is a point of the previous generation and the actual generation contains Point B, then the new position is a very favorable one: not only is B non-dominated by A, but B even dominates A. This kind of evolution is always desirable, and this transition certainly has to be preserved. If the evolutions brings A to C (or C′), the new point is, however, a non-dominated one; in this case, the transition

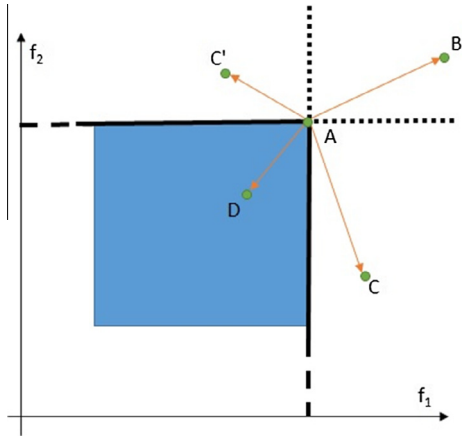

Fig. 2. The point A splits this two dimensional objectives space in two zones.

should also be preserved, in order to favor the spread of the points along the Pareto frontier. The elitism in this new version of the multi-objective genetic algorithm is applied as follows:

- MOGA II starts with the initial population P of size N and the elite set $E = 0$.
- For each generation, compute $P' = P \cup E$.
- If the cardinality of P' is greater than the cardinality of P, reduce P' removing randomly the exceeding points.
- Compute the evolution from P' to P'' applying all MOGA operators.
- Calculate the fitness for the population P''.
- Copy all non-dominated designs of P'' to E.
- Update E by removing duplicated or dominated designs.
- Resize the elite set E if it is bigger than the generation size N removing randomly.
- Return to step 2 considering P'' as the new P.

The final forms of equations defining the parameters C_i are following

$$C_1 = \rho_f^{-0.1333}\mu_f^{0.6924}\sigma_f^{1.7454}t_{inj}^{1.2643}p_{2,avg}^{-2.8836}n^{0.3265}p_c^{0.7624} \quad (26)$$

$$C_2 = \rho_f^{0.0027}\mu_f^{-0.1458}\sigma_f^{-0.8047}Q_c^{1.013}p_{2,avg}^{-0.8068}n^{-0.5301}p_c^{-0.2052} \quad (27)$$

$$C_3 = \rho_f^{-0.0231}\mu_f^{2.0129}\sigma_f^{-0.8263}t_{inj}^{-1.8602}p_{2,avg}^{-0.0413}n^{-0.5881}p_c^{1.2287} \quad (28)$$

$$C_4 = \rho_f^{-2.3932}\mu_f^{-0.4868}\sigma_f^{2.5949}t_{inj}^{1.5919}p_{2,avg}^{1.458}n^{0.2846}p_c^{-0.4263}d_z^{3.5505} \quad (29)$$

$$C_5 = \rho_f^{0.2517}\mu_f^{-0.0352}\sigma_f^{-0.1950}Q_c^{-1.2941}p_{2,avg}^{0.1066}n^{-0.013}p_c^{0.1566}d_z^{-0.5497} \quad (30)$$

where ρ_f is fuel density [kg/m^3], μ_f is fuel dynamic viscosity [MPa s], σ_f is fuel surface tension [N/mm], t_{inj} stands for injection time [ms], $p_{2,avg}$ is the average injection pressure [MPa], Q_c represents injection rate [mm^3/cycle], n is a pump speed [1/min], p_c pressure in the chamber [MPa] and d_z nozzle hole diameter [mm]. The dimensionless parameters in Eqs. (26)–(30) were inserted into the AVL Fire to close the mathematical model used for initial conditions of position, size, velocity, temperature, and the number of particles in the parcel and have the definite and significant impact on the development of spray and its characteristics.

5. Experiment setup

5.1. Spray visualization system

The system for spray visualization consists of the pressure chamber and two subsystems for pressure setup and for fuel spray visualisation. In Subsystem 1, the conventional reduction valve was used. The purpose of reduction valve was the setup of pressure in the pressure chamber to achieve the conditions that usually occur in combustion chambers. The pressure of 40 and 60 bars was set, and inert gas N_2 was used. Subsystem 2 consisted of Friedmann–Maier type 112H-100H test-bed, which allows the setting of pump rotation speed and a PES 6A 95D 410 LS 2542 BOSCH pump, with six BOSCH DLL 25S834 injection nozzles, each with one injection hole. One of the nozzles was mounted on the top of the pressure chamber. A high-speed camera was used to capture the images of spray development during the injection process in the pressure chamber. The system for spray visualization is schematically presented in Fig. 3.

5.2. Fastec HiSpec 4 high-speed camera

The spray images were captured with a Fastec HiSpec 4 high-speed digital camera. The camera was placed at a 1.7 m distance from the fuel spray. A resolution of 128 × 332 pixels and a frame-rate of 18,499 fps were used, based on spray shape and duration. The camera was triggered with a falling electric pulse that was acquired simultaneously with pressure p_1 and p_2, needle

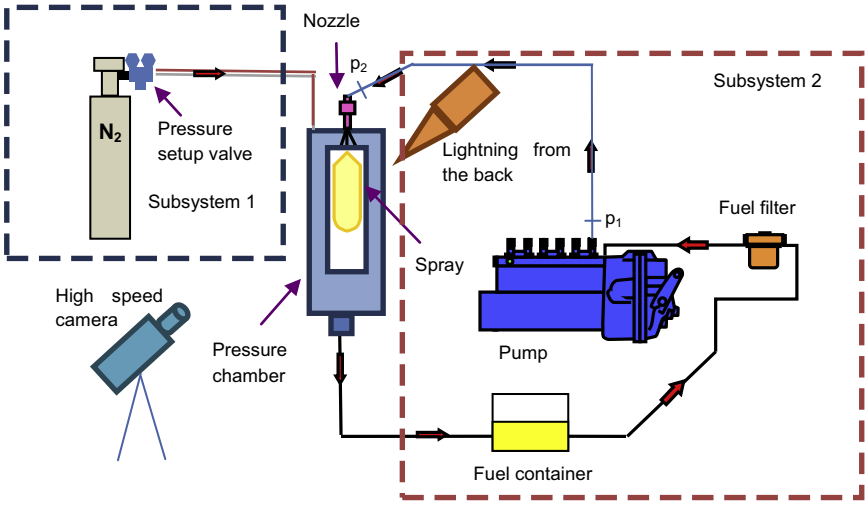

Fig. 3. Schematic diagram of system for spray visualisation.

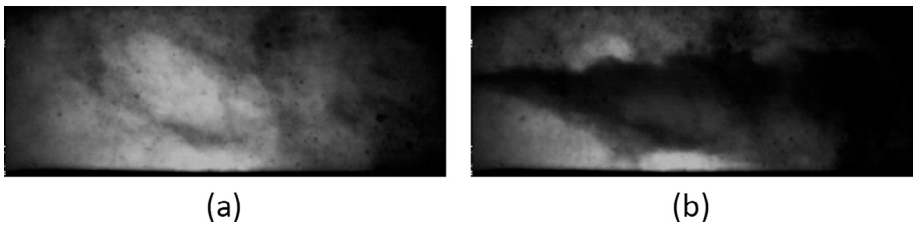

Fig. 4. Image of fuel fog before injection (a) and at needle closure (b).

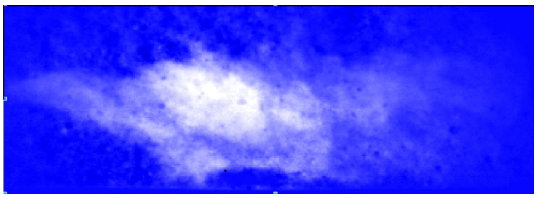

Fig. 5. Subtracted image.

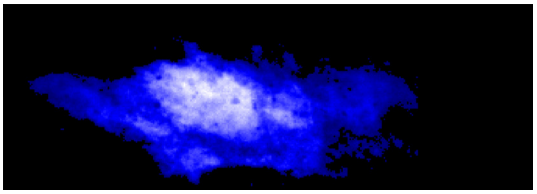

Fig. 6. Subtracted image with homogenous background.

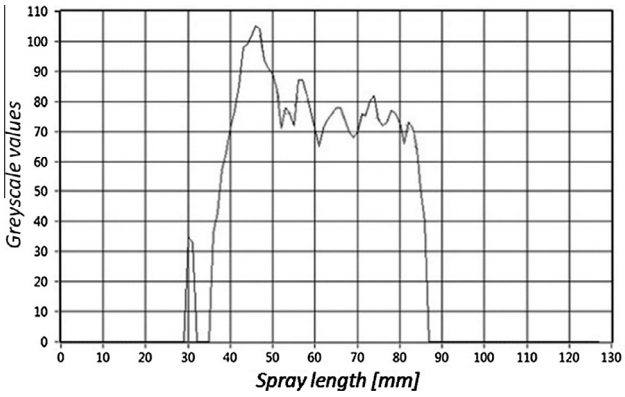

Fig. 7. Slice at 1/3 of spray length.

lift, and the signal for TDC (top dead centre) so that the time delay of the first recorded image could be defined.

5.3. The visualisation of fuel spray

Two different methods were used for spray visualisation. The first method for spray analyses, built in LabVIEW program, was used for determination of the spray cone angle and length. The second method enabled the calculation of the velocity on the spray border from the sequence of images taken.

5.3.1. Visualisation method for spray cone angle and length calculation

The fuel injection in the pressure chamber causes the breakup of the fuel into small droplets. These small droplets create a fuel fog, which makes it difficult to obtain the spray cone angle and length directly from images. The idea to improve the visual quality of the raw images is based on the presumption that the shape of the fog cloud remains the same during the injection. An additional issue that can be addressed with this approach is illumination inhomogeneity and spots on the chamber window. A raw image just before the injection started is presented in Fig. 4(a). Fig. 4(b) was taken just before needle closure.

All issues (illumination inhomogeneity, fog cloud and spots) are evident in Fig. 6. In order to obtain the actual spray cone angle and length, the greyscale values of both images were stored in a 2D matrix. A 2D matrix of greyscale values in Fig. 4(a) was subtracted from the 2D matrix greyscale values on Fig. 4(b). The subtracted image is presented in Fig. 5.

Furthermore, it is possible to perform a histogram analysis of the subtracted image and establish the border value for the background and to set up the maximum greyscale value to extract the greyscale interval with the highest interest, as presented in Fig. 6, where a homogeneous background can be noted.

The images taken were stored in a 2D matrix from which it is possible to extract a single raw/column. The whole image presented in Fig. 6 was sliced perpendicular to the spray propagation direction. An example of greyscale values at one third of spray length is shown in Fig. 7.

The greyscale data were fed into the subprogram where amplitude was observed. When amplitude value fell below the pre-set limit, the program stopped and returned the maximum spray length and the spray angle at one third of the maximal spray length.

5.3.2. Visualisation method for velocity field determination

The ADMflow [19,20] software method was developed in order to calculate the velocities of a fluid flow and is based on the assumption that in a chosen region of interest, the greyscale level A is proportional to the spray concentration N – Eq. (31). The term 'spray concentration' means the local spray thickness in the radial direction, to which the image brightness (grey level) is assumed to be proportional:

$$A_n \propto N \tag{31}$$

The same applies for the time derivatives

$$\frac{\Delta A}{\Delta t} \propto \frac{\partial N}{\partial t} \tag{32}$$

Because spray concentration is under consideration, Eq. (32) can be transformed into a form, known as advection–diffusion equation:

$$\frac{\partial N}{\partial T} + \frac{\partial (N v_x)}{\partial x} + \frac{\partial (N v_y)}{\partial y} = D\left(\frac{\partial^2 N}{\partial x^2} + \frac{\partial^2 N}{\partial y^2}\right), \tag{33}$$

D is the diffusivity and represents the proportionality coefficient between the flow of spray concentration due to diffusion, and the concentration gradient. v_x and v_y are the components of the spray velocity vector v [m/s] on a location within the region of interest:

$$v = (v_x, v_y) \tag{34}$$

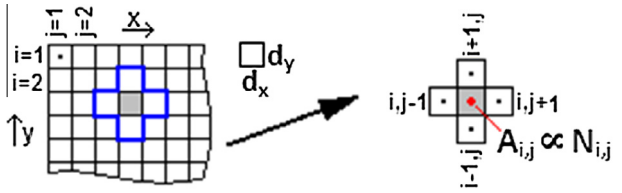

Fig. 8. Discretization scheme of recorded images.

The actual spray development process is three-dimensional, meaning that has three components, but due to our choice of the region of interest, the third velocity component is small in comparison to the other two and can be neglected. The length of the vector v is equal to the absolute velocity of spray:

$$v = \sqrt{v_x^2 + v_y^2} \tag{35}$$

The variable N and its partial derivatives are determined numerically on the basis of the measured greyscale level A at a given location (within the region of interest) and time [19,20]. The differential equation given by Eq. (33) can be reduced to a linear equation via transformation into a discrete form, i.e. Eq. (36). Spatial derivatives in Eq. (36) are discretized by the central difference method [19].

$$\frac{A_{i,j}(t+\Delta t) - A_{ij}(t)}{\Delta t} + \frac{(Av_x)_{i,j} - (Av_x)_{i,j-1}}{2d_x} + \frac{(Av_y)_{i,j} - (Av_y)_{i,j-1}}{2d_y} = D\left[\frac{A_{i,j+1} - 2A_{i,j} + A_{i,j-1}}{d_x^2} + \frac{A_{i+1,j} - 2A_{i,j} + A_{i-1,j}}{d_y^2}\right] \tag{36}$$

Δt is image sampling rate (time between two consecutive images), d_x and d_y are the horizontal and vertical dimensions [mm], respectively, of the base element for the greyscale level data acquisition within the region of interest. Theoretically, the smallest base element size is equal to the pixel size, $d_x = d_y = d_p$. The discretization scheme is shown by Fig. 8.

As a result of the discretization, the number of unknowns doubles and at least 5 consequent images are needed to solve the system of linear equations [19]. In cases in which more than 5 images are included in the calculation (40 consecutive images used here), the system of equations is over-determined and is solved by the least square method. For every image analyzed, a vector of instantaneous velocity is obtained as a solution. A larger number of images used in the calculation leads to a more stable solution, but also to a stronger averaging effect as the high frequency velocity oscillations are filtered out. Prior to the velocity calculation, images are processed by filters, such as the Gaussian filter, which reduces the effect of pixilation. In addition, flow equations used in our software contain user-adjustable regulation coefficients that control the effect of velocity gradient, divergence (proportional to flow compressibility) and curl (proportional to flow vorticity). Higher values of these coefficients mean that certain components of the flow equations are penalized to a greater extent.

6. Results and discussion

6.1. Validation of improved primary and secondary break-up models

The final forms of the equations defining the parameters of break-up models were implemented into the AVL FIRE solver. They were validated with the use of diesel and biodiesel fuel at chamber pressures of 40 and 60 bars at 800 rpm. The experimental and numerical simulation results comparison for the chamber pressure at 40 and 60 bars is presented in Figs. 9 and 10 and Tables 3 and 4.

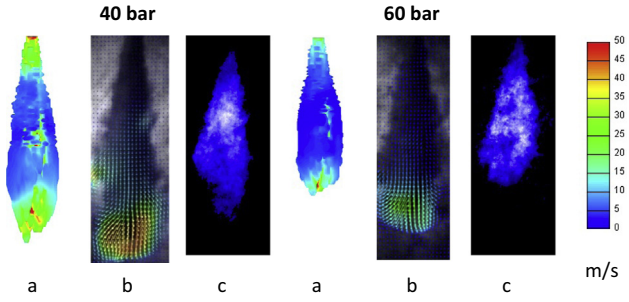

Fig. 9. Spray development (D2, 800 rpm, 40–60 bar): numerical results (a), AMDflow (b) and modified (c) image.

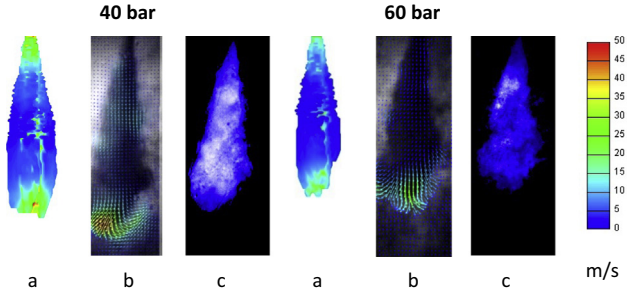

Fig. 10. Spray development (B100, 800 rpm, 40–60 bar) numerical results (a), AMDflow (b) and modified (c) image.

All presented results were taken at the same camshaft rotational angle, under the assumptions that the needle is fully opened, the spray is fully developed, and the spray velocities have reached the maximal values. Both velocity components were determined by computer-aided (AMDflow and AVL FIRE) visualization in the same measurement point in a x–y plane. A sequence of 40 successive images was used to define the flow velocity field in x–y plane. This number of images assured that the set in Eq. (31) was well defined in all points of interest. In contrast, averaging the velocity components over a large sequence requires more CPU time and may result in loss information. Nevertheless, there are some differences in length and orientation of velocity vectors between in both programs. A comparison of results presented in Table 5 confirms that that velocity values have similar forms regardless of the

Table 3
Differences of spray length between experimental and numerical simulation for various fuel types for 800 rpm at a chamber pressure of 40 and 60 bar.

Length (mm)	Chamber pressure (bar)			
	40		60	
Fuel	D2	B100	D2	B100
Camera	70	72	63	68
Simulation	69	71	61	66

Table 4
Differences of spray angle between experimental and numerical simulation for various fuel types for 800 rpm at a chamber pressure of 40 and 60 bar.

Spray angle (°)	Chamber pressure (bar)			
	40		60	
Fuel	D2	B100	D2	B100
Camera	30	35	32	36
Simulation	29	33	30	34

Table 5
Differences of average spray velocity vectors between experimental and numerical simulation for various fuel types for 800 rpm at a chamber pressure of 40 and 60 bar.

Spray velocity vectors (m/s)	Chamber pressure (bar)							
	40				60			
Fuel	D2		B100		D2		B100	
Axis	*x*	*y*	*x*	*y*	*x*	*y*	*x*	*y*
AMDflow	0.5302	4.3474	0.5534	4.8784	0.8829	3.9187	0.9541	4.3466
Simulation	0.5550	4.4773	0.5789	4.9283	0.9028	4.0487	0.9763	4.5668

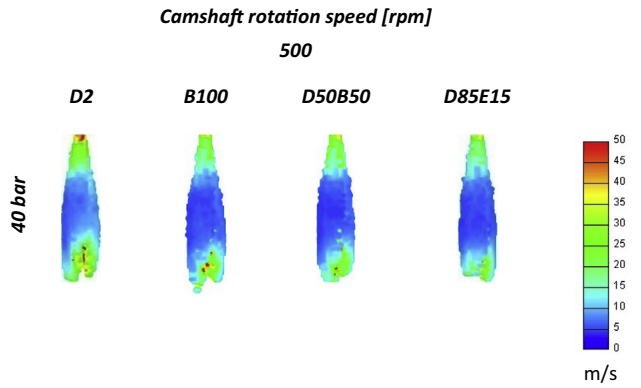

Fig. 11. Spray development for various fuels at a camshaft rotational speed of 500 rpm and at 40 bars.

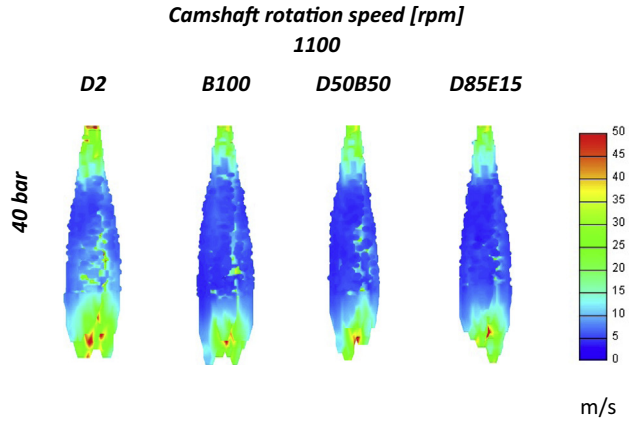

Fig. 12. Spray development for various fuels at a camshaft rotational speed of 1100 rpm and at 40 bars.

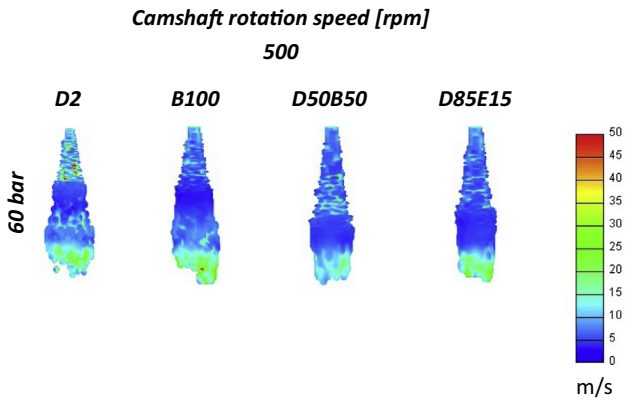

Fig. 13. Spray development for various fuels at a camshaft rotational speed of 500 rpm and at 60 bars.

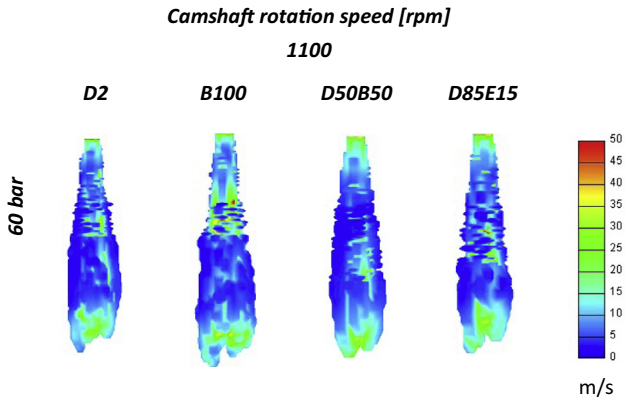

Fig. 14. Spray development various fuels at a camshaft rotational at camshaft rotational speed of 1100 rpm and 60 bars.

program used. The comparison of the results in Tables 3 and 4 shows good agreement in the spray development as well as in its shape (spray cone angle and penetration length). Spray simulation results confirm the adequacy of primary and secondary break-up parameter expressions for a conventional injection system.

6.2. Results of numerical simulations with improved primary and secondary break-up models

Based on the images of the spray visualization, we have determined one main spray development phase of interests, shown in Figs. 11–14 and Tables 6 and 7. The images show the spray development at different camshaft rotational speeds and for various biofuels. All the images represent the full development of spray.

The comparison shows good agreement in the spray shape (spray cone angle and length) and spray velocity. The differences between the results for different fuels are less than 10% for spray length and about 20% for spray cone angle. The differences in fuel physical properties results in the spray shape that is wider and longer for biodiesel fuel than for the D50B50 and D85E15 diesel fuel blends. The results also show that the spray length for biodiesel fuel is longer that for diesel fuel, for which the result for spray length and spray cone angle for the D50B50 blend lies between the values of pure diesel and biodiesel fuel. The higher density of the fuels used has some influence on the spray cone angle, which is usually wider for fuels with higher density. The ambient pressure in the chamber influences the spray length and the spray cone angle in such a way that the spray is shorter and wider for higher pressures in the chamber. The camshaft rotation speed has the most influence on spray length and spray cone angle. At higher camshaft rotation speeds, the spray is longer and narrower.

The results proved that the primary and secondary parameters have a major impact on the spray. The increase of parameter C_1 value increases spray penetration length, while the parameter C_3 determines the basic shape of the spray. The increase of the parameter C_2, which directly influences the droplet initial diameters and

Table 6
Differences of spray length and cone angle between numerical simulation for various fuel types for 500, 800 and 1100 rpm at a chamber pressure of 40 bars.

Fuel	Chamber pressure 40 (bar)					
	Spray length (mm) Camshaft rotation speed (rpm)			Cone angle (°) Camshaft rotation speed (rpm)		
	500	800	1100	500	800	1100
D2	56	69	79	30	29	28
B100	62	71	82	35	33	31
D50B50	58	70	76	33	31	29
D85E15	57	71	77	34	30	27

Table 7
Differences of spray length and cone angle between numerical simulation for various fuel types for 500, 800 and 1100 rpm at a chamber pressure of 60 bars.

Fuel	Chamber pressure 60 (bar)					
	Spray length (mm) Camshaft rotation speed (rpm)			Cone angle (°) Camshaft rotation speed (rpm)		
	500	800	1100	500	800	1100
D2	54	61	77	32	30	29
B100	56	66	80	39	34	32
D50B50	55	64	76	35	32	30
D85E15	54	63	74	36	31	28

velocities, generally decreases the spray angle and lengthens its penetration. Parameters C_4 and C_5 have noticeable impacts on spray cone angle and length. These two parameters have some influence only at lower camshaft rotational speeds. Increasing or decreasing the parameter C_4 and C_5 values has only minor influence on the length of spray penetration, but increases the CPU times for numerical simulations. The values of those two parameters should be close to zero to obtain the best results on spray development. The simulations have shown that the values of parameters C_4 in C_5 should be near the value zero that the values for spray cone angle and spray penetration length are comparable to experimental data, and the CPU time reaches the minimum value.

Nevertheless, the fuel physical properties and the engine operating conditions mostly influence the spray characteristics (shape, cone angle, and penetration length). The results for the improved primary and secondary models showed that with the fuel physical properties, operating conditions, and injection characteristics, the numerical model's empirical parameters can be expressed. The comparison of the spray cone angle, penetration length, and velocity profiles showed that the biofuels have similar spray shapes and characteristics to those of the standard diesel fuel. In particular, the differences in spray length at different camshaft rotation speeds are caused by different fuel physical properties; these have a significant impact on the injection characteristics. A higher fuel density and bulk modus increase the injection pressure, which is then reflected in better injection, spray velocity, cone angle and (usually) a larger penetration of the spray.

7. Conclusion

This paper discusses the influence of spray characteristics for different types of biofuel. The study is focused on numerical investigation of biofuels' influence on injected spray (cone angle and length) at various engine-operating regimes and different pressures. Several empirical parameters of primary and secondary breakup were modelled to enable faster and similar analysis of biofuels' spray shapes. The improved numerical model includes the influence of local flow conditions, fuel properties, operating parameters and the ambient pressure in a specially developed pressure chamber. For the validation of the improved numerical model, experimental investigations were made. The macroscopic spray developments were investigated in terms of spray tip penetration, spray cone angle, spray velocity using a spray visualization system under various experimental conditions (pressure chamber 40 or 60 bars) and different biofuel blends. The break-up parameters used in the model were modified for diesel, biodiesel fuel (produced from rapeseed oil) and the D50B50 and B85E15 blends in order to achieve experimentally obtained spray macro-characteristics. The nozzle used for the spray simulations had only one hole (only one spray tip penetration); with the visualisation method, only the spray cone angle, spray penetration length and spray velocity could be investigated. The improved numerical model makes the numerical simulations more general and predicts possible problems that could appear in diesel engines. The study indicates the possibility of replacing the mineral diesel fuels with different biofuels. To achieve more universal expressions, additional research should be conducted for several different injection systems and specifically nozzles.

Acknowledgments

This work was supported by Slovenian Research Agency (ARRS). We also wish to thank AVL LIST GmbH for their support by providing the AVL-AST software FIRE.

References

[1] Kegl B. Effects of biodiesel on emissions of a bus diesel engine. Bioresour Technol 2008;99:863873.
[2] Xue J, Grift TE, Hansena AC. Effect of biodiesel on engine performances and emissions. Renew Sustain Energy Rev 2011;15:10981116.
[3] Lešnik L, Vajda B, Žunič Z, Škerget L, Kegl B. The influence of biodiesel fuel on injection characteristics, diesel engine performance, and emission formation. Appl Energy 2013;111(11):558–70.
[4] Corpetti T, Heitz D, Arroyo G, Mémin É, Santa-Cruz A. Fluid experimental flow estimation based on an optical-flow scheme. Exp Fluids 2006;40:80–97.
[5] Torres Jimenez E, Pilar Dorado M, Kegl B. Experimental investigation on injection characteristics of bioethanol–diesel fuel and bioethanol–biodiesel blends. Fuel 2011;90(5):1968–79.
[6] Lee S, Tanaka D, Kusaka J, Daisho Y. Effects of diesel fuel characteristics on spray and combustion in a diesel engine. JSAE200224660. Tokyo, Japan: Japanese Society of Automotive Engineers; 2002.
[7] Choi CY, Bower GR, Reitz RD. Nozzle flow, primary diesel fuel break-up and spray formation with an Eulerian multi-fluid-model. In: ICLASS 2003. Sorento, Italy; 2003.
[8] Reitz RD, Diwaker J. Effect of drop break-up on fuel sprays. SAE 860469.
[9] Reitz RD, Hessel RP. Optimization of IC engine design for reduced emissions using CFD modelling. In: Selected papers from the THIESEL 2002 conference, Valencia, Spain; 11–13 September, 2002.
[10] Matsumoto A, Moore WR, Lai M-C, Zheng Y, Foster M, Xie X-B, Yen D, Confer K, Hopkins E. Spray characterization of ethanol gasoline blends and comparison to a CFD model for a gasoline. SAE international 2010-01-0601.
[11] Agarwal AK, Chaudhury VH. Spray characteristics of biodiesel/blends in a high pressure constant volume spray chamber. Exp Therm Fluid Sci 2012;42:212–8.
[12] Lee CS, Park SW, Kwon SI. An experimental study on the atomization and combustion characteristics of biodiesel-blended fuels. Energy Fuels 2005;19:2201.
[13] Grimaldi C, Postrioti L. SAE tech pap ser 2000, 2000-01-1252.
[14] Hohmann S, Renz U. Numerical simulations of fluid spray at high ambient pressure: the influence of real gas effects and gas solubility on droplet vaporisation. Int J Heat Mass Transfer 2003;46:3017–28.
[15] Suh HK, Park SH, Kim HJ, Lee CS. Influence of ambient flow conditions on the droplet atomization characteristics of dimethyl ether (DME). Fuel 2008. http://dx.doi.org/10.1016/j.fuel.2008.11.018.
[16] Pogorevc P, Kegl B, Škerget L. Diesel and biodiesel fuel spray simulations. Energy Fuels 2008;22:1266–74.
[17] AVL FIRE version 2013, Spray. AVL LIST Gmbh, Graz; 2013.
[18] Horn J, Nafpliotis N. Multiobjective optimisation using the Niched Pareto genetic algorithm, (Tech. Report), IlliGAL Report 93005. Illinois Genetic Algorithms Laboratory, University of Illinois; 1993.
[19] Bajcar T, Širok B, Eberlinc M. Quantification of flow kinematics using computer-aided visualization. Stroj Vestn 2009;55(4):215–23.
[20] Širok B, Bajcar T, Orbanić A, Eberlinc M. Melt mass flow measurement in mineral wool production. Glass Technol 2011;52(5):161–8.